Applied Physics B (2023) 129:91
https://doi.org/10.1007/s00340-023-08034-7

Applied Physics B
Lasers and Optics

RESEARCH

Material-specific high-order harmonic generation in laser-produced plasmas for varying plasma dynamics

Jan Mathijssen[1,2] · Zeudi Mazzotta[1,3] · Amelie M. Heinzerling[1,4] · Kjeld S. E. Eikema[1,2] · Stefan Witte[1,2]

Received: 9 December 2022 / Accepted: 2 May 2023 / Published online: 13 May 2023

Abstract
We present a new experimental setup for high-order harmonic generation in laser-produced plasmas, allowing the generation of coherent VUV and EUV light, as well as characterisation of the laser-produced plasmas by studying the emitted harmonics. We have successfully generated high-order harmonics in laser-produced Al, Ni, Ag, In, and Sn plasmas. Large differences in harmonic spectra and signal yields have been observed for these different targets. Harmonics up to order 25, corresponding to a wavelength of 62.4 nm and photon energy of 19.9 eV, have been measured with tin plasmas. Scanning laser parameters and delay between pump and fundamental laser pulses allows us to optimise the harmonic yield and observe the temporal dynamics of the laser-produced tin plasma.

1 Introduction

Next-generation nanolithography devices make use of extreme ultraviolet (EUV) radiation, emitted by a laser-produced plasma (LPP) in tin, to print nanometer-sized features on semiconductor wafers. Such LPPs are created by illuminating a target with intense laser radiation that ablates part of the target surface and forms a plasma. The properties of such LPPs are heavily dependent on the incident laser parameters. Additionally, the EUV radiation which is emitted by this plasma strongly depends on the plasma properties. A thorough understanding of the plasma dynamics and its influence on optical emission is therefore an important subject of study.

Many efforts have been spent in understanding the fundamental physics of EUV emission from tin LPPs, as well as the laser-matter interaction leading to the deformation of micrometer-sized tin droplets to more suitable EUV source targets [1, 2, 3]. The UV and EUV emission spectra of tin LPPs generated by lasers of various wavelengths have been measured to optimise the spectral purity and conversion efficiency of laser light to in-band EUV radiation [4, 5, 6]. Ion and debris studies have also been carried out to gain fundamental knowledge on the plasma conditions in the LPP EUV source, and to extend the industrial lifetime of collector optics close to the LPP [7, 8, 9].

High-order harmonic generation (HHG) in the LPP by an auxiliary femtosecond laser may serve as a new method to gain time-resolved information from the LPP expanding in the vacuum, since the nonlinear HHG process is highly sensitive to variations in plasma density. The highest achievable photon energy in the single atom response of HHG is given by the cutoff energy $E_C = 3.17 \cdot U_P + I_P$, where $U_P = 9.33738 \cdot 10^{-5} \cdot I[\mathrm{PW/cm^2}] \cdot \lambda^2[\mathrm{nm}]$ is the ponderomotive energy of the electrons in the drive laser field with intensity I and central wavelength λ, and I_P is the ionisation potential of the generation medium. The cutoff energy scales with the ionisation potential I_P, meaning that HHG spectra are also sensitive to the different ionic charge states in the LPP.

The concept of generating high-order harmonics (HHs) in LPPs started in 1992 by generating HHG in rare-gas like ions with high ionisation potentials to increase the cutoff energy [10]. Although these initial experiments did not lead to an increase of the cutoff energy due to mismatches in the phase between driving laser and its harmonics as well as

✉ Stefan Witte
s.witte@arcnl.nl

[1] Advanced Research Center for Nanolithography (ARCNL), Science Park 106, 1098 XG Amsterdam, The Netherlands

[2] Department of Physics and Astronomy, and LaserLab, Vrije Universiteit Amsterdam, De Boelelaan 1081, 1081 HV Amsterdam, The Netherlands

[3] Present Address: ASML Netherlands B.V., De Run 6501, 5504 DR Veldhoven, The Netherlands

[4] Present Address: Max Planck Institute for Quantum Optics, Hans-Kopfermann-Str. 1, D-85748 AG Garching, Germany

defocusing effects caused by the presence of free electrons, large progress in terms of HH yield and extending the cut-off energy has been made in the field of LPP-based HHG since then. Many elements have served as targets to generate HHs in LPPs with various yields in HH strength and spectra [11, 12, 13, 14]. The highest-order harmonic generated in Mn LPPs from a secondary plateau region was H107 and high conversion efficiencies up to $5 \cdot 10^{-5}$ for the 11–19th harmonics have been achieved in Zn LPPs [15]. Additionally, contrary to HHG in noble gases, the resonant enhancement of single HHs, where the strength of a single HH in the plateau region is enhanced up to two orders of magnitude compared to its neighboring HHs, has been observed in plasma HHG [16, 17, 18]. Such resonantly enhanced HHs with high flux and narrow bandwidth have great potential for diffraction-based experiments such as coherent diffractive imaging.

Although significant progress has been made in this field, experiments that focus on the influence of plasma composition on HHG have remained scarce. For this purpose, HHG experiments in more controlled LPPs with control over the plasma density and ionisation degree are needed. In this work, we present a new setup that allows systematic studies of the spatial and temporal properties of controlled LPPs from various targets. Conversely, this setup is capable of controlling the plasma formation to maximise the harmonic yield for various different targets. We present bright HHG in various LPPs and showcase the impact of changing plasma generation laser parameters on the HHG spectra. Firstly, we give a full description of the experimental setup. Secondly, the results for HHG in various LPPs, as well as the dynamics of HHG in tin plasmas are presented, followed by the discussion, outlook, and a conclusion.

2 Experimental setup for plasma-based high-order harmonic generation

The experimental setup for the generation and detection of HHG in LPPs consists of two major components, being the interaction chamber and the EUV spectrometer. A schematic of the vacuum system is shown in Fig. 1.

In the center of the interaction chamber, a solid metal target is mounted on a 4-dimensional translation stage (XYZR). The pump beam that creates the plasma is a high-energy Nd:YAG laser system with arbitrary sub-nanosecond pulse shaping capability [19]. This laser system outputs pulses with a flattop beam profile, a central wavelength of 1064 nm, pulses up to 1 µs duration with a shaping resolution of 0.43 ns and pulse energy up to 450 mJ at a repetition rate of 100 Hz. It is loosely focused to a spot size of 450 µm (e^{-2} diameter) on the target. For most of the experiments, the shortest possible pulse length of 430 ps is used to generate the LPP. In this case, the pump energy E_p is varied between 0.5 and 20 mJ, depending on the target. Longer 60 ns pulses were also used to create quasi-static LPPs where the plasma charge state composition could be tuned by varying the laser energy. In this latter case, similar pump energies of 5 mJ and 10 mJ were sent on the target to generate the plasma.

The solid target in the center of the interaction chamber is partially ablated with every pump pulse, leaving a crater at the surface of the target. When this crater becomes too

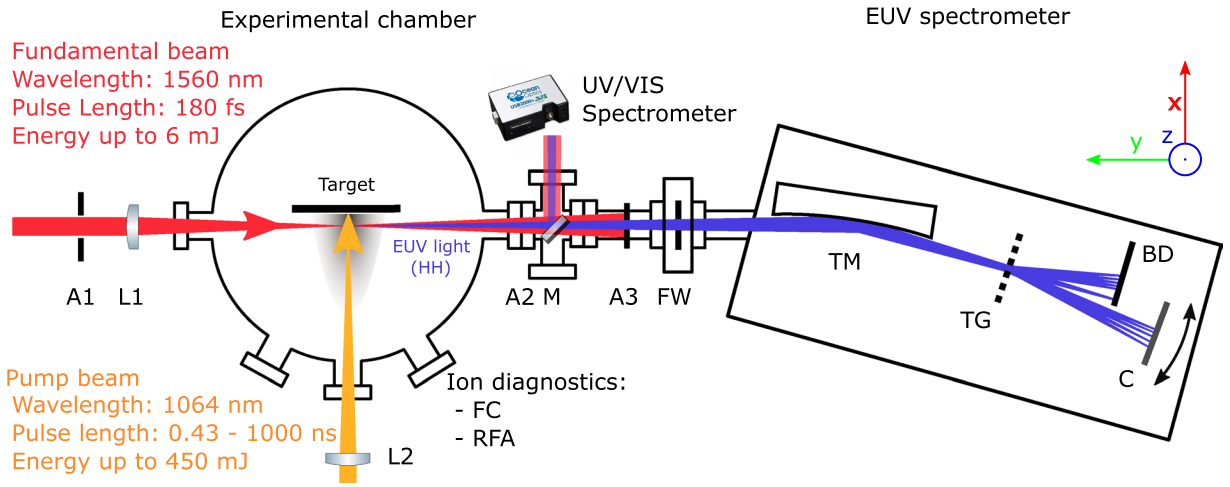

Fig. 1 A schematic of the vacuum setup, consisting of an interaction chamber where the plasma and high-order harmonics are generated, and an EUV spectrometer to analyze the high-order harmonics. *A* aperture, *L1*: $f = 300$ mm lens, *L2*: $f = 1000$ mm lens, *M* insertable mirror, *FW* filter wheel, *FC* faraday cup, *RFA* retarding field energy analyser, *TM* toroidal mirror, *TG* transmission grating, *BD* beam dump, *C* EUV camera

deep, the laser-target interaction geometry changes resulting in a plasma that is less suitable for generating HHs as has been previously observed by Hutchison et al. [20]. Therefore, the target is translated in the horizontal and vertical (Y and Z) direction to a fresh spot after every burst of 157 pump pulses. The EUV camera then acquires the HHG signal from the final 150 shots as the first seven pump pulses remove the native oxide layer from the target surface. Besides the crater formation process, debris from the plasma is slowly coating the outside walls of the vacuum chamber. This debris takes up to a few milliseconds to fully expand into the vacuum chamber, well before the next pulse arrives in the experiment. Part of the LPP debris ends up at the pump laser viewport, although we find that the high-intensity laser pulses drive a self-cleaning process, causing every consecutive laser pulse to remove most debris from the viewport again.

Additionally, the distance between the target and the fundamental beam can be varied by translating the target in the X direction up to 2 mm. As this translation is much smaller compared to the focal length of 1000 mm, the effect on the generated plasma is negligible. Together with the delay between the pump and fundamental pulses, this allows us to probe the expanding plasma plume both spatially and temporally.

2.1 Ion diagnostics

To get an indication of the ion charge states that are present in the plasma, a Faraday cup (FC) and a retarding field energy analyser (RFA) are mounted on the experimental chamber at a small 9° angle with respect to the pump beam. The FC measures ion time-of-flight (TOF) currents, but is insensitive to specific charge states. In combination with the distance between the target and the FC, the kinetic energy distribution of the ions can be obtained from these TOF measurements. Similar to the FC, the RFA also measures ion TOF currents, although it discriminates ions with $E_{kin}/z < U_{Ret}$ where E_{kin} is the kinetic energy of the ion, z its charge state, and U_{Ret} the voltage applied to the retarding field plate in the RFA. Thus by scanning the voltage applied to the RFA, such kinetic energy distributions can be obtained for all the charge states that enter the detector [21]. It should be noted that the actual charge state composition and their kinetic energy distributions might be different inside the plasma compared to the measured ions at the ion detectors, because of recombination processes in the expanding plasma. Nevertheless, significant differences in measured charge states and kinetic energies at the detectors provide evidence of a changed plasma composition.

2.2 High-order harmonic generation

After a delay $\Delta\tau$ with respect to the start of the pump pulse, the fundamental pulse is sent through the plasma to generate the high-order harmonics. This delay can be electronically varied without the need of an optical delay line, ensuring identical alignment for all delays. The fundamental or harmonic driving laser for this setup is a high-energy optical parametric chirped-pulse amplifier (OPCPA) system delivering ultrashort pulses down to 180 fs at a central wavelength of 1.55µm, with pulse energies up to 10 mJ at a repetition rate of 100 Hz [22]. After spatial filtering with an 800 µm aperture to clean up the beam profile, up to 8 mJ of fundamental pulse energy reaches the experiment of which typically up to 6 mJ is actually sent into the experimental chamber. It is focused into the plasma plume with a 300 mm lens to a spot size of 115 µm (e^{-2} diameter), resulting in a laser peak intensity up to $6 \cdot 10^{14}$ W/cm^2 in the plasma plume to generate the HHs.

2.3 EUV spectrometer

As the HHs travel collinear with the fundamental beam, the EUV spectrometer is mounted in the line of sight of the fundamental beam. A retractable mirror M can be inserted into the beamline to send the fundamental beam and its low-order harmonics out of the vacuum chamber. Here the alignment of the fundamental beam through the experimental chamber can be monitored with the aperture pair A1 and A2. The overlap between the plasma and the fundamental beam can then be optimised by maximising the third harmonic generation (THG) signal measured by the UV/VIS spectrometer as this signal is much stronger than the HHs and the acquisition time of the UV/VIS spectrometer is significantly shorter. Since the divergence of the HHs is typically lower than that of the fundamental beam, part of the fundamental beam is clipped by the final aperture A3 while transmitting most of the HH beam. A filter wheel (FW) is mounted behind the final aperture A3. This particular filter wheel can hold up to five different filters for transmitting the HHs in a specific spectral range while blocking the fundamental beam.

Within the EUV spectrometer chamber, a toroidal mirror under a grazing incidence angle of 7.5° is used to image the HH generation point onto the EUV camera (C) plane, with a demagnification of 1.8 to increase the spectral resolution. A grating mount holding up to three transmission gratings is placed between the toroidal mirror and the detector plane. The distance between the gratings and the detector plane equals 170 mm. These gratings are home-fabricated in collaboration with the AMOLF Nanolab cleanroom facility. For the fabrication, we sputter coat a 100 nm-thick gold layer on top of a free standing silicon nitride film with a thickness of

50 nm and a square clear aperture of 500 µm (Ted Pella). A binary grating containing several support structures is then patterned into the gold-coated film by means of a focused ion beam (FIB). For the current experiments, a transmission grating with a line density of 1000 mm^{-1} is mounted in the holder to disperse the frequency components of the HHs and the EUV plasma emission.

To measure harmonics in the wavelength range above 70 nm, no suitable metal filters are available, and therefore we measure these HHs without any filter in the beamline. Since the EUV camera is unable to handle the intensity of the fundamental IR beam, a beam dump (BD) is placed between the transmission grating and the EUV camera to block the 0th and -1st diffraction order. The remaining 1st order is transmitted to the EUV camera. Finally, the dispersed HHs and the plasma emission are collected and measured by an EUV camera (Greateyes GE 2048 512 BI UV3). This detector is mounted on a rotational stage, centered around the transmission grating. This allows us to conveniently rotate the camera to capture different spectral regions while keeping the distance between the grating and the EUV camera constant. Angles up to 18° with respect to the 0^{th} order can be reached in both directions. In combination with the 1000 mm^{-1} grating, this spectrometer allows us to measure a total wavelength span between 6 nm and 300 nm, while we can measure a range of 160 nm with a resolution around 1 nm in a single camera position. This resolution is limited by the clear aperture of the transmission grating and the imaging aberrations introduced by the toroidal mirror. The expected spectral widths of the HHs lie between 0.8 nm and 3 nm, and our spectrometer resolution is therefore sufficient to resolve the bandwidth of most HHs.

3 Results

To explore the capabilities and limitations of the setup, we first study HHG for various generation media. We then proceed to show the possibility for this experimental setup to function as a spatially and temporally resolved plasma diagnostic. Finally, we show the degree of control we can exert on the LPPs to systematically study the dependence of the HHG signal on the plasma composition.

3.1 HHG in various LPPs

In Fig. 2, we show the optimal HH spectra generated in LPPs from five different metals, namely aluminium, nickel, silver, indium, and tin. The motivation for these five materials lies in the differences in atomic weight and their differences in first and second ionisation potentials. An overview of the atomic numbers Z, the masses, and the ionisation potentials for all targets can be found in Table 1.

Table 1 Overview of atomic masses and ionisation potentials of the materials used for LPP-based HHG

Target	Z	Mass (U)	1st Ip (eV)	2nd Ip (eV)
Aluminium (Al)	13	26.98	5.98	18.8
Nickel (Ni)	28	58.69	7.63	18.2
Silver (Ag)	47	107.9	7.57	21.49
Indium (In)	49	114.8	5.79	18.9
Tin (Sn)	50	118.7	7.34	14.6

Ionisation energies obtained from [23]

Measured HHG spectra for all tested elements are displayed in Fig. 2. The bottom panel in each measurement shows a camera image from which the static background signals from the fundamental beam and pump beam have been subtracted. All these results are averages of recordings at 21 separate spots on the target, with 150 laser shots on each spot. The remaining background signal in the images can be attributed to the remainder of the fundamental beam and the HHs in the 0th order which are scattered from the beam dump onto the EUV camera. The top panel in each graph shows the vertically integrated signal from the central 15 pixels around the HHG signal on the EUV camera image after further subtracting the sum of 15 vertical pixels located 50 pixels below the HH signal to reduce the broad background signal contribution.

A first observation from Fig. 2 is that the HHG spectra vary strongly for different elements, and require significantly different laser parameters to optimize HHG spectrum and flux. The optimum HH spectrum obtained in aluminium plasma was generated with a pump energy of 8 mJ, a fundamental energy of 4 mJ and a delay between the two pulses of 30 ns. The highest-order harmonic detected in these experiments is H17 at a wavelength of roughly 92 nm or a photon energy of 13.6 eV. Noticeably, the strength of H7 is much brighter than that of its neighbouring harmonics, including the fifth harmonic. This observation might hint at a resonance enhancement effect, although further experiments are needed to verify this.

The pump energy and fundamental energy required to drive optimal HHG in nickel plasmas is similar to that of the aluminium case, namely 6 mJ and 4 mJ, respectively. Also the optimal delay of 30 ns is virtually identical to the aluminium case. The signal strength of the HHG in the nickel plasma is however more than two orders of magnitude lower compared to HHG in aluminium plasmas. The harmonic cutoff for HHG in nickel is also lower as the highest-order harmonic detected is H13.

For the case of silver, again similar laser energies were needed to drive HHG in the plasma plume. The optimum energies for pump and fundamental pulses were found to be 8 mJ and 2.5 mJ, respectively. Highest HHG yields were

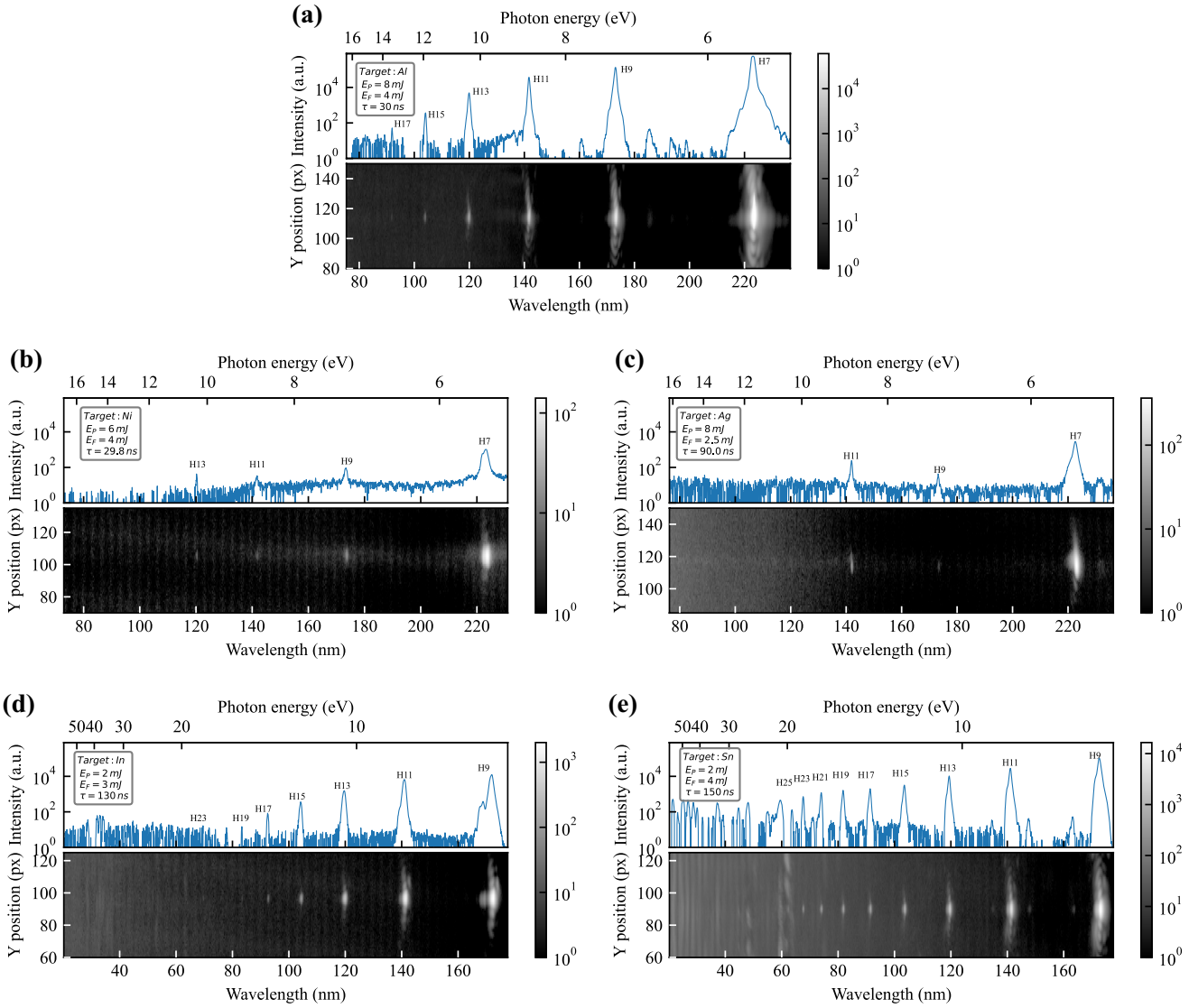

Fig. 2 Typical HHG spectra for the **a** Al, **b** Ni, **c** Ag, **d** In and **e** Sn targets. Experimental conditions can be found in the subfigure insets. All bottom panels show EUV camera images after subtraction of pump and fundamental background contributions. All top panels show vertically integrated spectra. Note that the HHG spectra for In and Sn have been acquired at a different EUV camera angle, shifting the spectral range of the spectrometer

observed around a delay of 90 ns. The fundamental beam was more strongly absorbed in the silver plasma compared to the other targets. Additionally, the HHG spectrum shows a lower H9 intensity compared to the intensities of harmonics seven and eleven. This might be explained by the presence of the $4d^9 5p$ to $4d^9 7s$ spectral line of Ag II at 172.4 nm. However, other spectral lines can also be found in the vicinities of H7 and H11, while these harmonics seem to be absorbed less. Another possible explanation for the weaker H9 might be that the HH spectrum is cutoff at H9 while H11 is resonantly enhanced, although more research is needed to confirm this.

Typical HHG spectra in indium reach up to H17 with the highest signal strength for the low-order harmonics at pump and fundamental energies of 4 mJ and 2.5 mJ, respectively. For a lower pump energy of 2 mJ, faint H19 and H23 signals are also observed. Contrary to the HHG signals observed in previous materials, In HHG spectra show a more plateau-like behaviour up to H19, similar to expected spectra from conventional HHG in noble gases. The optimal delay between pump and fundamental pulses was found to be 140 ns.

The highest-order harmonics up to H25 were generated in tin plasmas. For these HHG spectra, a relatively low pump energy of 2 mJ was needed in combination with a fundamental energy of 4 mJ and a delay of 150 ns. The harmonic

strength of H9 is comparable to that of H9 generated in aluminium, although the spectrum extends to much higher photon energies up to 19.9 eV. The HH intensity drops fast from H9 to H15, but a plateau region is observed up to H21, after which the HH intensity drops steeply again. Unfortunately, the harmonic spectrum has its cutoff below the expected resonance at a wavelength of 47.1 nm or photon energy of 26.3 eV [18].

Overall, large differences are observed in the material-dependant HHG spectra. These differences cannot simply be explained with the differences in atomic weights between the targets as high signal strengths are observed for both light elements such as aluminium as well as for heavier elements such as indium and tin. Furthermore, low signal strengths have also been observed for both the lighter nickel as well as the heavier silver target. Also the first and second ionisation potentials of the target do not seem to have a direct correlation with the HH strength. As most of the observed HH photon energies (except for tin) remain below the second ionization potential of the generation medium, a likely explanation is that most of the HHs are generated by neutral atoms rather than ions in the plasma.

3.2 HHG as plasma diagnostic

By varying the pump and fundamental laser energies as well as the delay between the two laser pulses, the HHG yield can be optimised, as the influence of these parameters on the local plasma properties results in different phase matching conditions. Vice versa, the HHG spectra at specific fundamental energies may therefore contain information on the plasma properties in which the HHs are generated. Figure 3 shows the tin LPP HH yield dependencies on pump energy and fundamental energy. From the pump energy scan, it can be seen that both the high-order harmonics and the low-order harmonics behave similarly, although the higher-order harmonics show a more pronounced decrease in signal strength at pump energies of 4 mJ and 6 mJ, hinting at slight differences in phase matching conditions between the high-order harmonics and the lower-order harmonics. Scanning the fundamental energy shows a steep increase in HH signal between 1 mJ and 2 mJ, after which this growth flattens resulting in stable HHG for higher fundamental energies. The HH signal scales more strongly for the higher-order harmonics. The brightness of H21 varies by more than two orders of magnitude, while the signal from the lower-order harmonics varies by only one order of magnitude.

This difference between lower-order and higher-order harmonics can be visualised even better with individual 2D intensity maps per harmonic for the full energy scan range, as shown in Fig. 4. The grey scales of these plots are individually normalised. Note that the signal strength of H21 is nearly two orders of magnitude lower than that of H9.

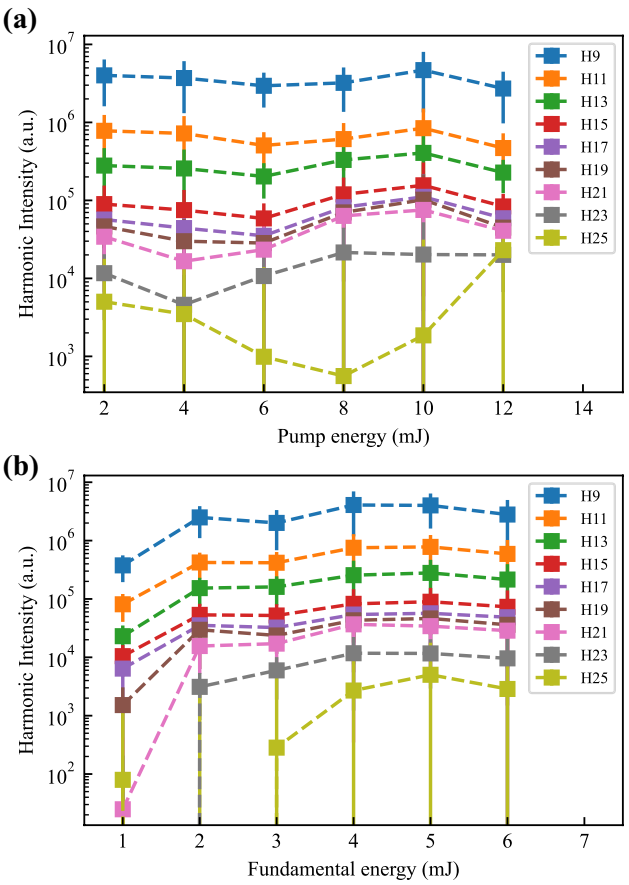

Fig. 3 **a** Pump energy scan for HHG intensity in tin plasmas at fundamental energy of 5 mJ and **b** fundamental energy scan for HHG intensity in tin plasmas at pump energy of 2 mJ

The harmonic yield for H9 and H13 vary less strongly as a function of pump and fundamental energies compared to H17 and H21.

From these plots it can be concluded that the brightness of all HHs peaks around pump and fundamental pulse energies of 10 mJ and 6 mJ, and that the higher-order HHs exhibit another local maximum at pump and fundamental energies of 2 mJ and 4 mJ, respectively. However, background signals due to e.g. scattered THG also increase for higher pump energies, which complicates background subtraction for the highest energies. The resulting lower signal to noise ratio is visible in the larger error bars for the highest pump energies in Fig. 3 a.

Scanning the delay between pump and fundamental pulses allows us to examine the temporal expansion dynamics of the tin LPP into the vacuum. The HH intensities as a function of delay are plotted in Fig. 5. The distance between the fundamental beam and the target is optimised for harmonic yield by barely grazing the target in this delay scan. The estimated distance between the target and the fundamental beam waist is roughly 150 µm. At short delays, no

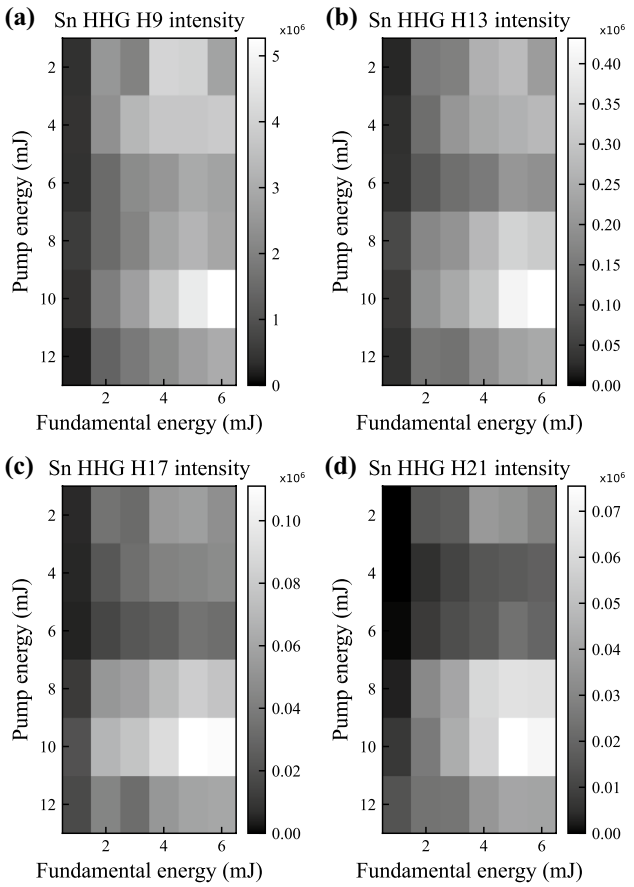

Fig. 4 HHG intensity dependence on fundamental energy and pump energy in Sn LPP for **a** H9, **b** H13, **c** H17, and **d** H21

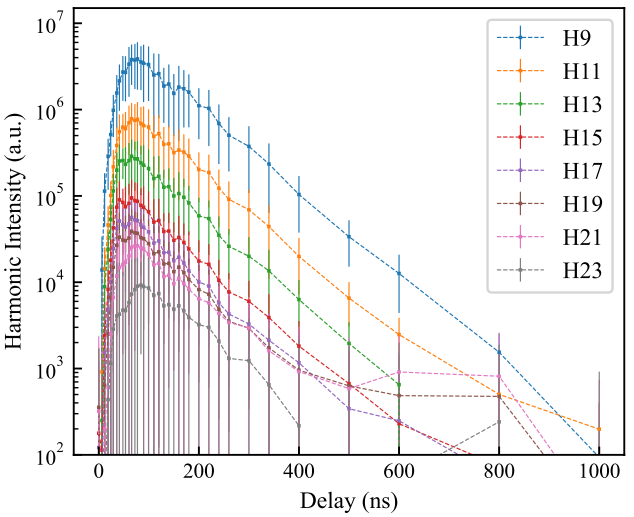

Fig. 5 Observed HH intensity as a function of time delay between pump and fundamental pulses, for HHG in tin LPP generated with 0.43 ns-long, 2 mJ pump pulses, at a fundamental pulse energy of 4 mJ

HH signal is observed since the LPP has not expanded far enough into the vacuum to reach the fundamental interaction region. In the first 100 ns, the HH signal grows nearly exponentially as the LPP is expanding into the vacuum and enters the interaction region. The intensity of all harmonics peaks around a delay of $\tau = 80$ns for this particular target-fundamental distance. After the optimum delay, the LPP expands even further into the vacuum and the medium density decreases, eventually becoming too low to efficiently generate HHs. In this expansion phase, the HH signal decays exponentially with delay. The decay rate of the HH intensities is largely identical for all HHs. We therefore conclude that in the present conditions, the main parameter that influences the yield for HHs up to order 23 is the density of the medium rather than phase matching effects.

3.3 Controlling the laser-produced plasma (changing charge state composition)

All of the above results have been measured with the shortest Gaussian pump pulse length of 0.43 ns. However, the pump laser for these experiments has unique pulse shaping capabilities that allow us to control the generation of the LPP with high accuracy. We exploit this capability by also studying LPP for a longer and square pump pulse with a duration of 60 ns.

For these longer pump pulses, changing the laser energy will influence the charge state composition in the LPP [24]. This allows us to see the effects of the charge state composition in the LPP on the HHG spectra. As a proof of principle, we have generated HHs in LPPs pumped with 5 mJ and 10 mJ pump laser energies. The ion kinetic energy distributions dQ/dE measured at various set retarding voltages U_{Ret} for these two cases are plotted in Figs. 6 a and b, respectively. Although these plots show the kinetic energy distributions of the ions flying off the plasma, no information about the neutrals can be extracted from these measurements. As the ratio between neutrals and ions would be valuable information relating to the HHG phase-matching, this ratio is subject to further study. Note that the voltages shown are set retarding voltages and the actual voltages applied to the retarding grid may vary slightly because of the limited resolution of the HV supply. At 5 mJ pump energy there is mainly one smooth curve visible, meaning that the LPP mostly contains only singly charged tin ions. At 10 mJ pump energy a double-peaked structure appears, which indicates the presence of both singly and doubly charged tin ions. Additionally, the measured ion current per kinetic energy is higher in the 10 mJ case, as more mass is ablated which results in a higher LPP density. Finally, the maximum kinetic energy of the ions produced with a 10 mJ pump beam is 2–3 times higher than those produced with a 5 mJ pump beam.

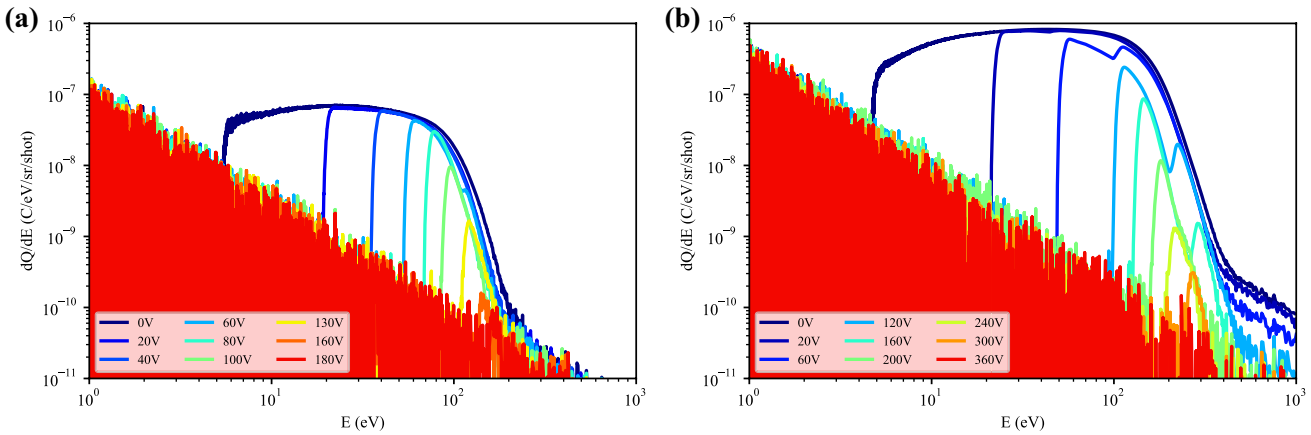

Fig. 6 Kinetic energy distributions of ions detected with a retarding field energy analyzer for **a** 5 mJ pump energy and **b** 10 mJ pump energy. Different curves correspond to the set retarding voltages U_{Ret} on the retarding grid

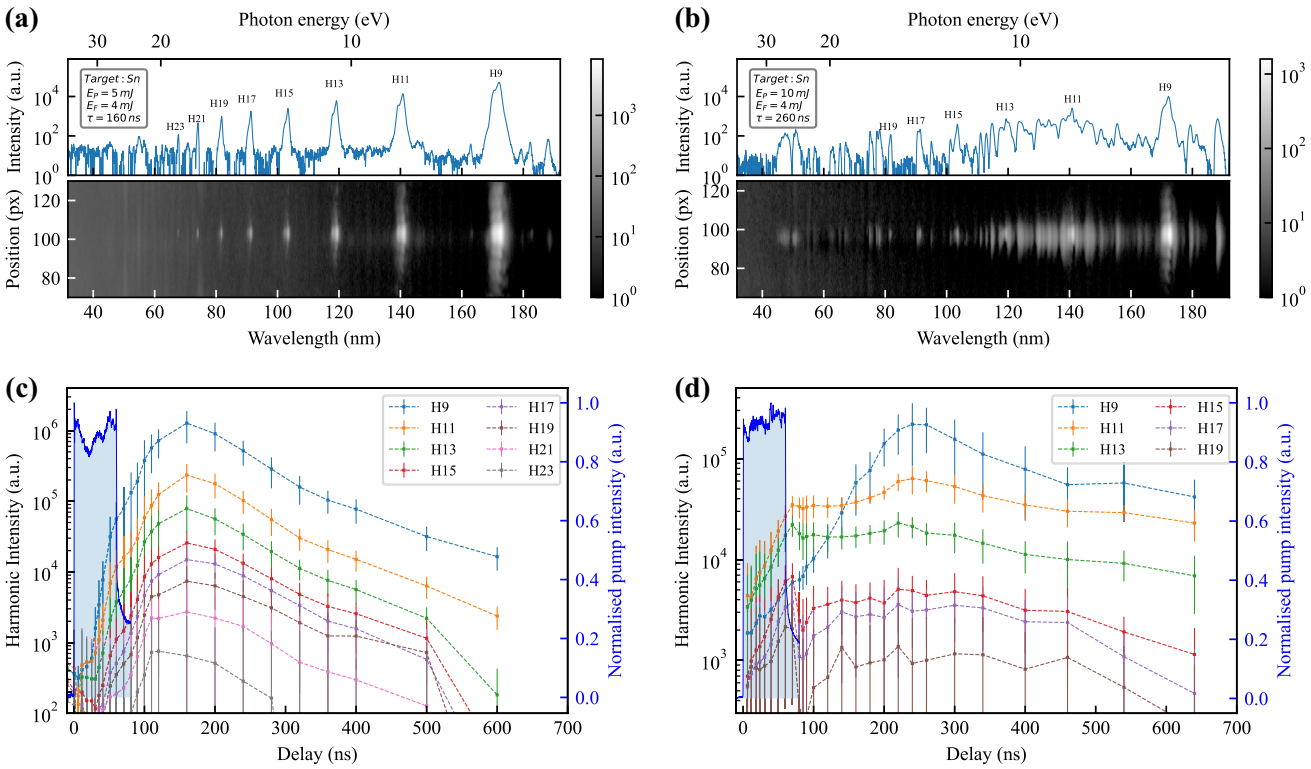

Fig. 7 HHG spectra for optimized generation conditions using **a** 5 mJ and **b** 10 mJ pump pulse energy at 60 ns pump pulse duration. The bottom row shows the observed HH intensity as a function of time delay between pump and fundamental, for the same pump energies of **c** 5 mJ and **d** 10 mJ. The blue shaded curves in **c** and **d** display the normalised temporal shape of the pump pulses. All HHG spectra and delay scans are generated with 4 mJ fundamental beam energy

We have generated HHs in these two distinct LPPs as a function of pulse delay to compare the dependence of the cutoff energy, the harmonic yield, as well as the temporal dynamics. The optimal HHG spectra for both pump energies are shown in Figs. 7 a and b, respectively. With the 60 ns pump pulses at 5 mJ energy, the measured HH intensity is roughly four times lower compared to the HH signal generated in the LPP pumped with 0.43 ns pulses. For this low pump energy case, the observed HHG spectrum remains quite bright and harmonics up to order 23 are observed, which is comparable to the shorter pump pulse case. Similar observations on the HHG cutoff with respect to

the pump pulse length have been made by Ganeev et. al [25]. For these longer pump pulses, the pump laser energy has a more pronounced effect on the HH cutoff and intensity. Only HHs up to order 19 were observed when using 10 mJ, 60 ns pump pulses, whereas the highest observed harmonic for the 10 mJ, 0.43 ns pump beam was H23. The observed HH signal strength is significantly lower at 10 mJ pump energy compared to the 5 mJ case. One reason for this decrease in HH signal is the increased fundamental absorption in the higher-density LPP. This increased absorption also leads to a temperature rise in the LPP, resulting in a higher ionisation fraction and increased EUV-UV emission, which appears as a multitude of spectral lines that form a background to the measured HHG signals in Fig. 7b.

The HH intensities as a function of delay pumped with the 60 ns-long pulses of 5 mJ and 10 mJ are shown in Figs. 7 c and d, respectively. The blue shaded curves display the normalised temporal shape of the pump laser. The slowly decaying tail of these curves can be attributed to the electronic response of the photodiode rather than the actual pump intensity. The pump-to-fundamental time-delay dependence of the HHG also shows markedly different behaviour for the 5 mJ and the 10 mJ pump energies, as can be seen in Figs. 7 c and d. At 5 mJ pump energy, the HH signal starts rising after roughly 30 ns delay time. This HHG onset delay is much longer compared to the 0.43 ns pump pulse cases where HH signal appears from delays of $\tau = 10$ns onwards. After a steep increase up to roughly 60 ns, the signal keeps growing until it peaks around 160 ns. Afterwards, as the plasma expands into the vacuum its density decreases, leading to a decrease in HH intensity as well.

For the $E_P = 10$ mJ case, the fundamental pulse leads to a more rapid heating of the LPP, resulting in an apparent signal increase in the first tens of nanoseconds as seen in Fig. 7d, which however is mainly caused by incoherent background emission from the plasma rather than actual harmonics. The actual HH signal appears above this background after a delay of 130 ns after which it peaks around 260 ns. The decrease in signal strength for the 10 mJ case is much slower compared to the 5 mJ case. Weak HH signals were observed up to delays of 1.6 µs, whereas at 5 mJ pump energy the maximum delay for which HH signals remained visible was 1.0 µs.

4 Discussion and outlook

The highest-order harmonics generated in our five different targets remained well below values reported in literature [12, 14, 16, 17]. Considering the maximal ponderomotive energy from the peak intensity of the fundamental laser pulses $U_P = 45$ eV for a pulse energy of 4 mJ, much higher-order harmonics could be expected, although plasma effects such as electron defocusing are likely to reduce the actual peak intensity in the plasma. In addition, phase matching effects may be expected to dominate the observed HHG spectrum rather than the single-atom response: free electrons in the plasma and the additional ionization in the leading edge of the relatively long fundamental pulse can therefore also be a cause for the observed HHG cutoff. To this end, it is simplistic but insightful to consider the barrier suppression intensity above which atoms or ions are further ionised [12], which would lead to the generation of significant amounts of free electrons that generally inhibit phase matching. In the case of aluminium, the barrier suppression intensity above which all neutral Al will be ionised is $1.0 \cdot 10^{13}$W/cm^2. At a central wavelength of 1560 nm, this corresponds to a ponderomotive energy of $U_P = 2.24$ eV. From this, the single atom response predicts a cutoff energy of $E_C = 3.17 \cdot U_P + I_P = 13.2$eV, which is 16.5 times the photon energy of the fundamental. As this number nearly matches the highest-order harmonic observed with a photon energy of 13.6 eV, it seems reasonable to assume that the observed HHs are generated from neutral Al atoms rather than ions.

Continuing this reasoning, the expected cutoff energies for neutral nickel, silver, indium and tin are 13.1 eV, 10.7 eV, 7.6 eV and 10.1 eV, respectively. These cutoff energies are calculated assuming a barrier suppression intensity scaling of $F_{BSI} = \frac{I_P^2}{4Z}$ [26]. The observed HH cutoff energies in our experiments were 10.4 eV, 8.8 eV, 15.2 eV and 20 eV for Ni, Ag, In and Sn, respectively. From this simple model, we can expect to generate HHs mostly in neutrals for Al, Ni and Ag LPPs, while HHs from singly charged ions can be generated in In and Sn LPPs. However, the harmonic cutoffs for In and Sn do not scale according to a single-atom law with the second ionisation potential either, making it apparent that phase matching still dominates HHG in these elements. In general, a better model is needed to predict whether the HHs are generated from neutrals or ions. Furthermore, shorter fundamental pulses are likely to improve HHG yield as well.

In our energy scans with the HHG in Sn LPPs, we observe variations in HHG signal strength that allow optimizing the yield of individual HHs. For now the observed variations in HHG spectra are too small to consider this a quantitative plasma diagnostic, although we obtained a bright HH signal up to H25.

The delay scans measured with both the 0.43 ns-long pump pulses and the 60 ns-long pump pulses show large differences in HHG spectra. Especially the differences between the two pump energies for the 60 ns-long pulses are very pronounced, whereas this effect was much less noticeable for the 0.43 ns pump pulses. This difference is probably due to the more efficient plasma heating for the 60 ns pulses, leading to an overly dense plasma for efficient HHG.

While the available parameter space especially in terms of pump pulse properties is much larger, the present set of

experiments already showcases the capabilities of our LPP-based HHG setup. The present experiments clearly show some characteristics of the expanding LPPs generated by laser pulses of two different pulse lengths. More advanced experiments on HHG in LPPs generated with various temporal laser shapes in combination with ion diagnostics will be performed in future experiments, to systematically characterise these LPPs and optimise HHG yield. Through these experiments, we aim to provide a better understanding of the generation mechanisms and dominant charge states involved in the HHG process.

5 Conclusion

We have shown a new experimental setup capable of successfully generating HH radiation of a fundamental laser with a central wavelength of 1560 nm in various LPPs. Large differences in both HH yield and harmonic cutoff energy have been observed which cannot be explained by only considering differences in atomic number and the first and second ionisation potentials of the target species. HHG in aluminium LPPs has shown a very bright H7 compared to neighbouring harmonics H5 and H9, which may hint to the presence of a resonance enhancement. HHG in tin LPPs has shown the highest-order harmonic of H25 with a bright overall harmonic yield. Energy scans for pump and fundamental lasers have shown differences in harmonic yield and differences in phase matching for different harmonics. A delay scan with the 0.43 ns-long pump pulse has shown an increase in HH yield as the plasma expands into the interaction region, after which the further expansion dilutes the LPP to densities where no efficient HHG is possible. Finally, very different LPP expansion dynamics were observed for the 60 ns-long pump pulses with low and high energy compared to the 0.43 ns-long pump pulses.

Acknowledgements The authors thank Nik Noest for technical support, Lucas Poirier for his contribution to the RFA data analysis, and Dr. Aneta Stodolna and Tiago de Faria Pinto for their contribution to the development of the setup. This work has been carried out at the Advanced Research Center for Nanolithography (ARCNL), a public-private partnership of the University of Amsterdam, the Vrije Universiteit Amsterdam, the Netherlands Organization for Scientific Research (NWO) and the semiconductor equipment manufacturer ASML.

Author Contributions JM and SW designed research. JM, ZM and AMH conducted the experimental work. JM analyzed data, wrote the main manuscript text and prepared all figures. All authors reviewed and contributed to the manuscript.

Declarations

Conflict of interest The authors declare that they have no conflict of interest.

References

1. D. Kurilovich, T. de Faria Pinto, F. Torretti, R. Schupp, J. Scheers, A.S. Stodolna, H. Gelderblom, K.S.E. Eikema, S. Witte, W. Ubachs, R. Hoekstra, O.O. Versolato, Phys. Rev. Appl. **10**, 54005 (2018). https://doi.org/10.1103/PhysRevApplied.10.054005
2. T. de Faria Pinto, J. Mathijssen, R.A. Meijer, H. Zhang, A. Bayerle, D. Kurilovich, O.O. Versolato, K.S.E. Eikema, S. Witte, Appl. Phys. A (2021). https://doi.org/10.1007/s00339-020-04207-9
3. R.A. Meijer, D. Kurilovich, K.S.E. Eikema, O.O. Versolato, S. Witte, J. Appl. Phys. **131**(10), 105905 (2022). https://doi.org/10.1063/5.0082352
4. R. Schupp, F. Torretti, R.A. Meijer, M. Bayraktar, J. Scheers, D. Kurilovich, A. Bayerle, K.S.E. Eikema, S. Witte, W.M.G. Ubachs, R. Hoekstra, O.O. Versolato, Phys. Rev. Appl. **12**, 014010 (2019). https://doi.org/10.1103/PhysRevApplied.12.014010
5. Z. Bouza, J. Byers, J. Scheers, R. Schupp, Y. Mostafa, L. Behnke, Z. Mazzotta, J. Sheil, W.M.G. Ubachs, R. Hoekstra, M. Bayraktar, O.O. Versolato, AIP Adv. **11**(12), 125003 (2021). https://doi.org/10.1063/5.0073839
6. L. Behnke, R. Schupp, Z. Bouza, M. Bayraktar, Z. Mazzotta, R.A. Meijer, J. Sheil, S. Witte, W.M.G. Ubachs, R. Hoekstra, O.O. Versolato, Opt. Express **29**(3), 4475 (2021). https://doi.org/10.1364/OE.411539http://opg.optica.org/oe/abstract.cfm?URI=oe-29-3-4475
7. A.S. Stodolna, T. de Faria Pinto, F. Ali, A. Bayerle, D. Kurilovich, J. Mathijssen, R. Hoekstra, O.O. Versolato, K.S.E. Eikema, S. Witte, J. Appl. Phys. **124**(5), 053303 (2018)
8. L. Poirier, A. Lassise, Y. Mostafa, L. Behnke, N. Braaksma, L. Assink, R. Hoekstra, O.O. Versolato, Appl. Phys. B **128**(7), 135 (2022). https://doi.org/10.1007/s00340-022-07844-5
9. B. Liu, D. Kurilovich, H. Gelderblom, O.O. Versolato, Phys. Rev. Appl. **13**, 024035 (2020). https://doi.org/10.1103/PhysRevApplied.13.024035
10. Y. Akiyama, K. Midorikawa, Y. Matsunawa, Y. Nagata, M. Obara, H. Tashiro, K. Toyoda, Phys. Rev. Lett. **69**, 2176 (1992). https://doi.org/10.1103/PhysRevLett.69.2176
11. R.A. Ganeev, M. Suzuki, M. Baba, H. Kuroda, T. Ozaki, Opt. Lett. **30**(7), 768 (2005). https://doi.org/10.1364/OL.30.000768http://opg.optica.org/ol/abstract.cfm?URI=ol-30-7-768
12. R.A. Ganeev, M. Suzuki, M. Baba, H. Kuroda, J. Modern Optics **53**(10), 1451 (2006). https://doi.org/10.1080/09500340600552265
13. R.A. Ganeev, M. Suzuki, M. Baba, H. Kuroda, J. Opt. Soc. Am. B **22**(9), 1927 (2005). https://doi.org/10.1364/JOSAB.22.001927http://opg.optica.org/josab/abstract.cfm?URI=josab-22-9-1927

14. R.A. Ganeev, M. Baba, M. Suzuki, H. Kuroda, Phys. Lett. A **339**(1), 103 (2005). https://doi.org/10.1016/j.physleta.2005.02.073
15. R.A. Ganeev, M. Baba, M. Suzuki, S. Yoneya, H. Kuroda, J. Appl. Phys. (2014). https://doi.org/10.1063/1.4905188
16. R.A. Ganeev, M. Suzuki, M. Baba, H. Kuroda, T. Ozaki, Opt. Lett. **31**(11), 1699 (2006). https://doi.org/10.1364/OL.31.001699http://opg.optica.org/ol/abstract.cfm?URI=ol-31-11-1699
17. M. Suzuki, M. Baba, R. Ganeev, H. Kuroda, T. Ozaki, Opt. Lett. **31**(22), 3306 (2006). https://doi.org/10.1364/OL.31.003306http://opg.optica.org/ol/abstract.cfm?URI=ol-31-22-3306
18. M.A. Fareed, V.V. Strelkov, N. Thiré, S. Mondal, B.E. Schmidt, F. Légaré, T. Ozaki, Nat. Communicat. **8**(1), 16061 (2017). https://doi.org/10.1038/ncomms16061
19. R.A. Meijer, A.S. Stodolna, K.S.E. Eikema, S. Witte, Opt. Lett. **42**(14), 2758 (2017). https://doi.org/10.1364/OL.42.002758http://opg.optica.org/ol/abstract.cfm?URI=ol-42-14-2758
20. C. Hutchison, R.A. Ganeev, T. Witting, F. Frank, W.A. Okell, J.W.G. Tisch, J.P. Marangos, Opt. Lett. **37**(11), 2064 (2012). https://doi.org/10.1364/OL.37.002064http://opg.optica.org/ol/abstract.cfm?URI=ol-37-11-2064
21. L. Poirier, A. Bayerle, A. Lassise, F. Torretti, R. Schupp, L. Behnke, Y. Mostafa, W.M.G. Ubachs, O.O. Versolato, R. Hoekstra, Appl. Phys. B **128**(3), 39 (2022). https://doi.org/10.1007/s00340-022-07767-1
22. T. de Faria Pinto, J. Mathijssen, K.S.E. Eikema, S. Witte, Opt. Express **27**(21), 29829 (2019). https://doi.org/10.1364/OE.27.329829
23. A. Kramida, Yu. Ralchenko, J. Reader, and NIST ASD Team. NIST Atomic Spectra Database (ver. 5.10), [Online]. Available: https://physics.nist.gov/asd [2022, November 29]. National Institute of Standards and Technology, Gaithersburg, MD. (2022)
24. O.O. Versolato, Plasma Sources Sci. Technol. **28**(8), 083001 (2019). https://doi.org/10.1088/1361-6595/ab3302
25. R.A. Ganeev, M. Suzuki, M. Baba, H. Kuroda, Phys. Rev. A **76**, 023805 (2007). https://doi.org/10.1103/PhysRevA.76.023805
26. N.B. Delone, V.P. Krainov, Physics-Uspekhi **41**(5), 469 (1998). https://doi.org/10.1070/pu1998v041n05abeh000393